

Under consideration for publication in J. Fluid Mech.

The sandpaper theory of flow–topography interaction: The non-local formulation

Timour Radko^{1,†}, Justin Brown¹, Xiaobiao Xu², and Eric P. Chassignet²

¹Department of Oceanography, Naval Postgraduate School, Monterey, CA 93943, USA

²Center for Ocean-Atmospheric Prediction Studies, Florida State University, Tallahassee, FL 32310, USA

(Received xx; revised xx; accepted xx)

The irregular variability of the seafloor on lateral scales of several kilometers can strongly influence large-scale oceanic flows. However, these fine topographic patterns are currently unresolved by global circulation models and will remain subgrid in the foreseeable future. To address this complication, we develop the non-local "sandpaper" model of flow–topography interaction. This theory uses asymptotic multiscale methods to parameterize the effects of small-scale bathymetry in analytical and coarse-resolution numerical models. The previously reported version of the sandpaper theory assumed that the direct effects of bottom roughness are limited to the deepest density layer. Its reliance on the local approximation fundamentally restricted the model's ability to represent the vertical structure of abyssal flows. To overcome this deficiency, we develop a more general non-local model, in which the effects of bottom roughness are distributed throughout the water column. The non-local formulation opens a pathway for implementing the sandpaper closure in isopycnal models designed for realistic simulations, where density interfaces frequently intersect bathymetry. Local closure in such regions exhibits unphysical singularities, whereas its non-local counterpart remains well-behaved. The non-local sandpaper model is implemented in HYCOM (HYbrid Coordinate Ocean Model), one of the mainstream oceanographic general circulation models. The parameterization is tested on the canonical vortex spin-down problem. It is shown to be more accurate and applicable to a wider range of geophysical configurations than its local counterpart.

Keywords: ocean circulation, topographic effects

1. Introduction

The impact of irregular small-scale topography on large-scale circulation patterns in the ocean can be surprisingly profound. Particularly striking are the cumulative effects of bathymetric patterns with a lateral extent of several kilometers, commonly referred to as seafloor roughness. Typical heights of these topographic features can be as small as tens of meters—on the order of one percent of the total ocean depth. Yet, they tangibly affect currents commensurate in strength to the Gulf Stream and Kuroshio (*LaCasce et al.*, 2019). Several studies have emphasized the adverse impact of seafloor roughness on baroclinic instability of surface-intensified flows (*Palóczy and LaCasce*, 2022; *Radko*, 2024). As a result, rough topography can control the intensity and spatial distribution of transient mesoscale variability, which dominates the kinetic energy budget of the World Ocean

[†] Email address for correspondence: tradko@nps.edu

(e.g., *Stammer, 1997*). Seafloor roughness has also been invoked as a key factor in extending the lifespan of ocean rings and their ability to transport heat, nutrients, and pollutants across ocean basins (*Gulliver and Radko, 2022*).

However, despite the persistent stream of evidence implicating small-scale topography in various oceanic phenomena, our understanding of the basic physics at play remains limited. For instance, much attention has been paid to the effects of topographic pressure torque (*Hughes and de Cuevas, 2001; Jackson et al., 2006; Stewart et al., 2021*). An alternative, less explored mechanism of the interaction of broad currents with rough terrain involves the Reynolds stresses. When primary flows impinge upon small-scale bathymetric features, they inevitably generate eddies that modify the primary currents by laterally transferring momentum. For moderately swift flows, this mechanism of topographic control proved to be more effective than the bottom form drag (*Radko, 2023a,b*). Even such traditional assumptions as a monotonically increasing relation between the bottom drag and flow speed have been challenged. An argument has been made that, in certain regimes, the roughness-induced drag is inversely proportional to the velocity of abyssal currents (*Radko, 2023a,b*), implications of which could be substantial.

The limited insight into dynamics can also compromise more pragmatic objectives of the flow-topography interaction studies. Of particular concern is the representation of the effects of rough topography in numerical Earth System Models (e.g., *Mashayek, 2023*). Despite continuous advancements in high-performance computing, kilometer-scale bathymetric features and associated fine flow patterns are not even close to being resolved by global predictive systems. Given the undeniable significance of roughness, the only resort in the foreseeable future is the parameterization of its impact on larger scales of motion.

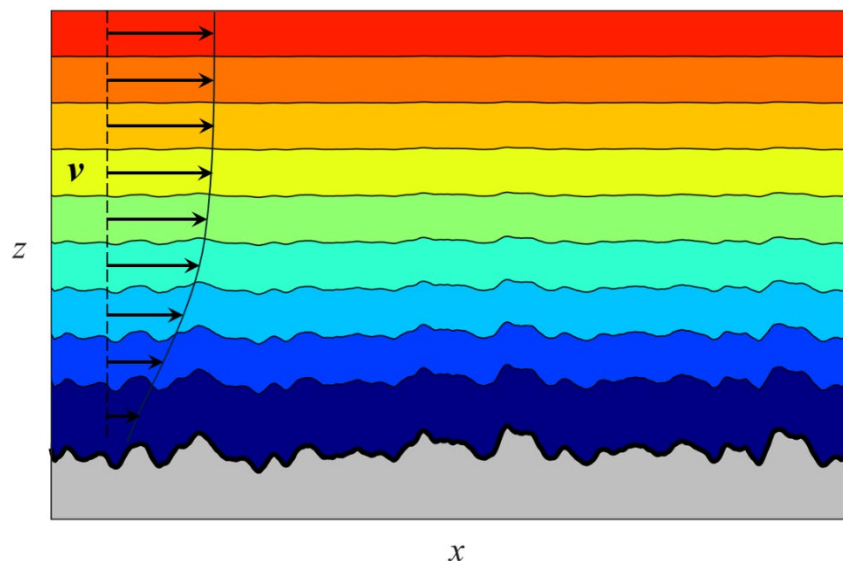


Figure 1. Schematic diagram illustrating the interaction of multilayer flows with rough topography. When the bottom layer thickness is less than the height of the direct influence of roughness, the small-scale variability in seafloor relief perturbs several interfaces in the abyssal zone. This small-scale variability leads to the systematic forcing of larger scales of motion in the affected layers.

A promising development in this area is the sandpaper theory of flow-topography interaction—see *Radko (2024)* and references therein. The model is based on the asymptotic expansion in a small parameter (ϵ) quantifying the scale separation between processes that we wish to parameterize and those that we intend to resolve. It uses conventional techniques of multiscale homogenization theory (e.g., *Vanneste, 2000, 2003; Mei and Vernescu, 2010; Goldsmith and Esler,*

2021) to formulate evolutionary equations for large-scale flows. The key strength of the sandpaper theory lies in its focus on statistical spectral properties of the seafloor relief (*Goff and Jordan, 1988; Goff, 2020*), which are expected to be more universal than patterns of topography in physical space. Because sandpaper theory is explicit and dynamically transparent, it holds promise to concurrently elucidate key mechanisms at play and offer parameterizations for coarse-resolution models.

While earlier versions of the sandpaper model succeeded in capturing key large-scale effects of roughness (*Radko, 2022a,b, 2023a,b*), its present state leaves room for further development. Perhaps the most severe restriction on the model's applicability is posed by the local approximation of topographic forcing. Currently, the sandpaper theory is formulated for multilayer isopycnal systems. From the outset, it assumes that roughness can directly influence only the deepest density layer. This assumption is valid for systems in which the bottom layer occupies a large fraction of the water column. However, the local approximation becomes highly suspect when the bottom layer is too shallow to contain the entire region directly affected by roughness. The schematic in Fig. 1 illustrates the principal complication. When layers are sufficiently thin, rough topography perturbs several density interfaces in the abyssal zone, generating kilometer-scale variability in velocity and layer thickness fields. In each affected layer, this variability produces the eddy form drag and Reynolds stresses that, in turn, influence larger scales of motion.

Thus, the local sandpaper theory ignores a potentially significant contribution to roughness-induced forcing from layers not directly in contact with topography. A difficult choice must be made to implement the local parameterization in isopycnal models. Users can either adopt a configuration with an exceedingly deep bottom layer, which permits only a crude representation of stratification, or *a priori* dismiss potentially important non-local components of topographic forcing. Since neither option is particularly appealing, we now develop a non-local sandpaper theory, in which the effects of roughness are distributed throughout the entire water column. The associated parameterization is implemented in HYCOM (HYbrid Coordinate Ocean Model)—a popular generalized vertical coordinate ocean circulation model used for climate prediction, operational forecasting, and process-oriented studies (*Bleck, 2002; Chassignet et al., 2003, 2006, 2009; Metzger et al., 2014*). We test the sandpaper closure on the canonical vortex spin-down problem against the corresponding roughness-resolving simulations.

The material is organized as follows. The governing multilayer shallow-water equations are presented in Sec. 2. Sec. 3 describes the development of the non-local sandpaper theory. In Sec. 4, the theory-based parameterization of roughness is implemented in HYCOM and validated by topography-resolving simulations. The results are summarized, and conclusions are drawn, in Sec. 5.

2. Formulation

The governing equations are based on the multilayer shallow-water model (e.g., *Pedlosky, 1987*):

$$\begin{cases} \frac{\partial \mathbf{v}_i^*}{\partial t^*} + (\mathbf{v}_i^* \cdot \nabla) \mathbf{v}_i^* + (-f^* \mathbf{v}_i^*, f^* u_i^*) = -\frac{1}{\rho_0^*} \nabla p_i^* + \nu^* \nabla^2 \mathbf{v}_i^* - \delta_{ni} \gamma^* \frac{\mathbf{v}_i^*}{h_i^*} + \delta_{1i} \frac{\boldsymbol{\tau}^*}{\rho_0^* h_i^*} \\ \frac{\partial h_i^*}{\partial t^*} + \nabla \cdot (\mathbf{v}_i^* h_i^*) = 0. \end{cases} \quad (2.1)$$

The asterisks denote dimensional quantities, $\mathbf{v}_i^* = (u_i^*, v_i^*)$ is the lateral velocity in layer $i = 1, \dots, n$, p_i^* is pressure, ρ_0^* is the reference density of the Boussinesq approximation, ν^* is the eddy viscosity, f^* is the Coriolis parameter, δ_{ij} is the Kronecker delta, $\boldsymbol{\tau}^* = (\tau_x^*, \tau_y^*)$ is the wind stress, and γ^* the bottom drag coefficient.

4

The shallow-water model also assumes the hydrostatic balance, which connects the dynamic pressure in adjacent layers:

$$p_i^* = p_{i+1}^* + g(\rho_{i+1}^* - \rho_i^*) \sum_{j=1}^i h_j^*, \quad i = 1, \dots, n-1. \quad (2.2)$$

The number of controlling parameters is reduced by non-dimensionalizing governing equations as follows:

$$\mathbf{v}_i^* = f_0^* L^* \mathbf{v}_i, \quad p_i^* = \rho_0^* (f_0^* L^*)^2 p_i, \quad (x^*, y^*) = L^* (x, y), \quad t^* = \frac{t}{f_0^*}, \quad h_i^* = H_0^* h_i, \quad (2.3)$$

where L^* , H_0^* , and f_0^* are the representative scales for the width of small-scale topographic features, vertical extent of the model, and the Coriolis parameter, respectively.

The non-dimensional momentum and thickness equations take the form

$$\begin{cases} \frac{\partial \mathbf{v}_i}{\partial t} + (\mathbf{v}_i \cdot \nabla) \mathbf{v}_i + (-fv_i, fu_i) = -\nabla p_i + \nu \nabla^2 \mathbf{v}_i - \delta_{ni} \gamma_b \frac{\mathbf{v}_i}{h_i} + \delta_{1i} \frac{\boldsymbol{\tau}}{h_i} \\ \frac{\partial h_i}{\partial t} + \nabla \cdot (\mathbf{v}_i h_i) = 0, \end{cases} \quad i = 1, \dots, n \quad (2.4)$$

where

$$\boldsymbol{\tau} = \frac{\boldsymbol{\tau}^*}{\rho_0^* L^* f_0^{*2} H_0^*}, \quad \nu = \frac{\nu^*}{L^{*2} f_0^*}, \quad \gamma = \frac{\gamma^*}{f_0^* H_0^*}. \quad (2.5)$$

The recursive relation (2.2) reduces in non-dimensional units to

$$p_i = p_{i+1} + B_{i,i+1} \sum_{j=1}^i h_j^*, \quad i = 1, \dots, n-1, \quad (2.6)$$

where $B_{i,i+1} = \frac{g^* (\rho_{i+1}^* - \rho_i^*) H_0^*}{\rho_0^* (f_0^* L^*)^2}$ is the Burger number.

The development of the sandpaper theory centers on the potential vorticity (PV) equation. It is obtained by taking the curl of the momentum equations (2.4), which eliminates the pressure gradient terms, and combining it with the thickness equation:

$$\frac{\partial q_i}{\partial t} + u_i \frac{\partial q_i}{\partial x} + v_i \frac{\partial q_i}{\partial y} = F_{qi}. \quad (2.7)$$

The relative and potential vorticities are denoted as $\zeta_i = \frac{\partial v_i}{\partial x} - \frac{\partial u_i}{\partial y}$ and $q_i = \frac{f + \zeta_i}{h_i}$, respectively.

Quantity F_{qi} on the right-hand side of (2.7) represents processes affecting the Lagrangian conservation of PV:

$$F_{qi} = \nu \frac{\nabla^2 \zeta_i}{h_i} - \delta_{ni} \frac{\gamma}{h_n} \nabla \times \left(\frac{\mathbf{v}_n}{h_n} \right) + \delta_{1i} \nabla \times \left(\frac{\boldsymbol{\tau}}{h_1} \right). \quad (2.8)$$

To perform the asymptotic multiscale analysis, we introduce the scale-separation parameter

$$\delta = \frac{L^*}{L_{LS}^*} = \frac{1}{L_{LS}} \ll 1, \quad (2.9)$$

where L_{LS} is the representative lateral extent of the large-scale flow. For convenience, we shall also use a related small parameter

$$\varepsilon \equiv \delta^{\frac{1}{2}}. \quad (2.10)$$

These parameters define the new set of spatial scales (X, Y) that reflect the dynamics of large-scale processes, which are related to the original ones as follows:

$$(X, Y) = \delta(x, y) = \varepsilon^2(x, y). \quad (2.11)$$

The derivatives in the governing equations are replaced accordingly:

$$\frac{\partial}{\partial x} \rightarrow \frac{\partial}{\partial x} + \varepsilon^2 \frac{\partial}{\partial X}, \quad \frac{\partial}{\partial y} \rightarrow \frac{\partial}{\partial y} + \varepsilon^2 \frac{\partial}{\partial Y}. \quad (2.12)$$

The elevation of the seafloor relative to its global mean level is denoted as $\eta = 1 - H$, where H is the total ocean depth, which is equal to the sum of individual layer thicknesses:

$$\sum_{i=1}^n h_i = H = 1 - \eta. \quad (2.13)$$

We assume that the seafloor elevation varies on both large and small scales. To isolate its large-scale (η_L) and small-scale (η_S) components, η is written as

$$\eta = \eta_L(X, Y) + \eta_S(X, Y, x, y). \quad (2.14)$$

where

$$\eta_L = \langle \eta \rangle, \quad \eta_S = \eta'. \quad (2.15)$$

The angle brackets represent averaging over small-scale variables and primes denote the deviation from the mean: $a' \equiv a - \langle a \rangle$.

The subsequent developments also make use of the Parseval identity (*Parseval, 1806*):

$$\langle ab \rangle = \iint \tilde{a} \cdot \text{conj}(\tilde{b}) dk dl, \quad (2.16)$$

where tildes denote Fourier images. The Fourier transform is defined as follows:

$$a = \frac{\sqrt{L_x L_y}}{2\pi} \iint \tilde{a}(k, l) \exp(ikx + lly) dk dl, \quad (2.17)$$

where (k, l) are the wavenumbers in x and y , and (L_x, L_y) is the domain size. The sandpaper model considers statistically isotropic small-scale components of bathymetry and therefore

$$|\tilde{\eta}_S|^2 = F_\eta(X, Y, \kappa), \quad (2.18)$$

where $\kappa \equiv \sqrt{k^2 + l^2}$.

3. The multiscale analysis

3.1. Fast flows

The non-local sandpaper model utilizes standard methods of multiscale mechanics (e.g., *Mei and Vernescu, 2010*) and bears some similarity to its local counterpart (*Radko, 2024*). Therefore, we present an abbreviated description of the model, focusing on the asymptotic sector with $U = O(\varepsilon)$ and $\nu = O(\varepsilon^2)$. This regime is characterized asymptotically large Reynolds numbers $\text{Re} = \frac{L^* U^*}{\nu^*} = O(\varepsilon^{-1})$, and the solutions obtained for this sector will be referred as the fast-flow model. The temporal variable is rescaled as $T = \varepsilon \delta t = \varepsilon^3 t$, which captures the advective timescale, and the time derivatives in governing equations are replaced by

$$\frac{\partial}{\partial t} \rightarrow \varepsilon^3 \frac{\partial}{\partial T}. \quad (3.1)$$

The Coriolis parameter is uniquely determined by large-scale meridional coordinate $f = f(Y)$, while the forcing and dissipative parameters are rescaled as follows:

$$\nu = \varepsilon^2 \nu_0, \quad \gamma = \varepsilon^2 \gamma_0, \quad \tau = \varepsilon^2 \tau_0. \quad (3.2)$$

The expansion opens with the $O(\varepsilon)$ large-scale velocity field in each layer ($i = 1, \dots, n$):

$$\mathbf{v}_i = \varepsilon \mathbf{v}_i^{(1)}(X, Y, T) + \sum_{j=2}^{\infty} \varepsilon^j \mathbf{v}_i^{(j)}(X, Y, x, y, T). \quad (3.3)$$

The corresponding pressure field takes the form

$$p_i = \varepsilon^{-1} p_i^{(-1)}(X, Y, T) + p_i^{(0)}(X, Y, T) + \varepsilon p_i^{(1)}(X, Y, T) + \sum_{j=2}^{\infty} \varepsilon^j p_i^{(j)}(X, Y, x, y, T), \quad (3.4)$$

and the analogous notation is used for the potential vorticity series. The Burger number in the recursive relation (2.6) is considered to be an $O(1)$ quantity. The small-scale bathymetric variability is weak:

$$\eta_s = \varepsilon^2 \eta_{s0}, \quad (3.5)$$

and the solution for thickness is sought in terms of power series

$$h_i = h_i^{(0)}(X, Y, T) + \varepsilon h_i^{(1)}(X, Y, T) + \sum_{j=2}^{\infty} \varepsilon^j h_i^{(j)}(X, Y, x, y, T). \quad (3.6)$$

The series for (u_i, v_i, h_i) are substituted into the governing equations and terms of the same order combined. The analysis commences by considering the leading-order perturbation balances. In the potential vorticity equation (2.7), the small-scale components emerge first at $O(\varepsilon^3)$:

$$\frac{\partial q_i^{(0)}}{\partial T} + u_i^{(1)} \frac{\partial q_i^{(2)}}{\partial x} + v_i^{(1)} \frac{\partial q_i^{(2)}}{\partial y} + u_i^{(1)} \frac{\partial q_i^{(0)}}{\partial X} + v_i^{(1)} \frac{\partial q_i^{(0)}}{\partial Y} = 0, \quad (3.7)$$

where $q_i^{(0)} = \frac{f}{h_i^{(0)}}$, and

$$q_i^{(2)} = \frac{1}{h_i^{(0)}} \left(\frac{\partial v_i^{(2)}}{\partial x} + \frac{\partial v_i^{(0)}}{\partial X} - \frac{\partial u_i^{(2)}}{\partial y} - \frac{\partial u_i^{(0)}}{\partial Y} - h_i^{(1)} q_i^{(1)} - h_i^{(2)} q_i^{(0)} \right). \quad (3.8)$$

We form the perturbation equations by subtracting the full equations and their (x, y) averages. For (3.7) we arrive at

$$u_i^{(1)} \frac{\partial q_i^{(2)}}{\partial x} + v_i^{(1)} \frac{\partial q_i^{(2)}}{\partial y} = 0, \quad (3.9)$$

whereas for (3.8) we obtain

$$q_i^{(2)} = \frac{1}{h_i^{(0)}} \left(\frac{\partial v_i^{(2)}}{\partial x} - \frac{\partial u_i^{(2)}}{\partial y} - h_i^{(2)} q_i^{(0)} \right). \quad (3.10)$$

To satisfy (3.9), we use $q_i^{(2)} = 0$, which reflects the homogenization tendency of potential vorticity (e.g., *Rhines and Young, 1982; Dewar, 1986; Marshall et al., 1999, Radko, 2022a,b*), reducing (3.10) to

$$\frac{\partial v_i^{(2)}}{\partial x} - \frac{\partial u_i^{(2)}}{\partial y} - \frac{f h_i^{(2)}}{h_i^{(0)}} = 0. \quad (3.11)$$

The $O(\varepsilon^4)$ PV balance is treated in a similar manner, which yields

$$u_i^{(1)} \frac{\partial q_i^{(3)}}{\partial x} + v_i^{(1)} \frac{\partial q_i^{(3)}}{\partial y} = -u_i^{(2)} \frac{\partial q_i^{(0)}}{\partial X} - v_i^{(2)} \frac{\partial q_i^{(0)}}{\partial Y} + \frac{v_0}{h_i^{(0)}} \nabla^2 \zeta_i^{(2)} - \frac{\gamma_0}{h_i^{(0)2}} \zeta_i^{(2)}, \quad (3.12)$$

where

$$q_i^{(3)} = \frac{1}{h_i^{(0)}} \left(\frac{\partial v_i^{(3)}}{\partial x} + \frac{\partial v_i^{(0)}}{\partial X} - \frac{\partial u_i^{(3)}}{\partial y} - \frac{\partial u_i^{(0)}}{\partial Y} - h_i^{(2)} q_i^{(1)} - h_i^{(3)} q_i^{(0)} \right). \quad (3.13)$$

The leading order perturbation momentum equations are

$$\begin{cases} f v_i^{(2)} = \frac{\partial p_i^{(2)}}{\partial x} \\ f u_i^{(2)} = -\frac{\partial p_i^{(2)}}{\partial y}. \end{cases} \quad (3.14)$$

Using (3.11) and (3.14), we connect the perturbation pressure and thickness:

$$\nabla^2 p_i^{(2)} = \frac{f^2 h_i^{(2)}}{h_i^{(0)}}, \quad (3.15)$$

which, in turn, yields the velocity components

$$\begin{cases} \nabla^2 u_i^{(2)} = -\frac{f}{h_i^{(0)}} \frac{\partial h_i^{(2)}}{\partial y} \\ \nabla^2 v_i^{(2)} = \frac{f}{h_i^{(0)}} \frac{\partial h_i^{(2)}}{\partial x}. \end{cases} \quad (3.16)$$

The leading-order small-scale component of the recursive relation (2.6) takes the form,

8

$$p_i^{(2)} = p_{i+1}^{(2)} + B_{i,i+1} \sum_{j=1}^i h_j^{(2)}, \quad (3.17)$$

whereas (2.13) reduces to

$$\sum_{i=1}^n h_i^{(2)} = -\eta_{S0}. \quad (3.18)$$

The system (3.15), (3.17), and (3.18) represents a closed set of linear equations that can be used to infer the pattern of the small-scale thickness $h_i^{(2)}$. We Fourier-transform this system in small-scale variables (x,y) and eliminate $\tilde{p}_i^{(2)}$, which results in

$$\begin{cases} \frac{f^2 a_i}{\kappa^2 h_i^{(0)}} - \frac{f^2 a_{i+1}}{\kappa^2 h_{i+1}^{(0)}} + B_{i,i+1} \sum_{j=1}^i a_j = 0, & i = 1, \dots, n-1 \\ \sum_{i=1}^n a_i = 1, \end{cases} \quad (3.19)$$

where a_i is the small-scale thickness component normalized by the seafloor roughness:

$$a_i = -\frac{\tilde{h}_i^{(2)}}{\tilde{\eta}_{S0}}. \quad (3.20)$$

Eqs.(3.19) make it possible to determine, for any given large-scale stratification, the distribution of small-scale perturbations throughout the water column. The array a_i represents the vertical attenuation of small-scale signatures of topography. The local model (*Radko, 2024*) assumes that the effects of seafloor roughness are limited to the lowest layer, which is equivalent to assigning $a_i = \delta_{ni}$. In contrast, the present formulation permits finite values of a_i in all layers, making it possible to explore the non-local large-scale effects of seafloor roughness. In this study, we also consider isotropic patterns of bottom roughness (2.18). Thus, (3.19) and (3.20) imply that small-scale patterns of attenuation coefficients are isotropic: $a_i = a_i(X, Y, T, \kappa)$. This, in turn, indicates that small-scale patterns of layer thickness and pressure are statistically isotropic as well.

Having determined the leading-order perturbation components, we now proceed to formulate large-scale equations. To that end, we average the governing system in x and y , focusing on the transfer of momentum and density by small-scale eddies. Considering (3.14) and (3.15), we conclude that

$$\left\langle u_i^{(2)} \frac{\partial u_i^{(2)}}{\partial x} \right\rangle = \left\langle v_i^{(2)} \frac{\partial u_i^{(2)}}{\partial y} \right\rangle = \left\langle u_i^{(2)} \frac{\partial v_i^{(2)}}{\partial x} \right\rangle = \left\langle v_i^{(2)} \frac{\partial v_i^{(2)}}{\partial y} \right\rangle = \left\langle u_i^{(2)} h_i^{(2)} \right\rangle = \left\langle v_i^{(2)} h_i^{(2)} \right\rangle = 0. \quad (3.21)$$

Thus, the small-scale eddy forcing terms emerge first at $O(\varepsilon^5)$ in the momentum equations and $O(\varepsilon^7)$ in the thickness equation. The mean fifth-order momentum equation takes the form

$$\frac{\partial \langle \mathbf{v}_i^{(2)} \rangle}{\partial T} + \mathbf{A}_i^{(5)} + \mathbf{R}_i^{(5)} + \left(-f \langle v_i^{(5)} \rangle, f \langle u_i^{(5)} \rangle \right) = -\nabla_x \langle p_i^{(3)} \rangle - \delta_{ni} \gamma_0 \frac{\langle \mathbf{v}_n^{(3)} \rangle}{h_n^{(0)}}, \quad (3.22)$$

where $\nabla_x \equiv \left(\frac{\partial}{\partial X}, \frac{\partial}{\partial Y} \right)$ denotes the large-scale gradient, and $\mathbf{A}_i^{(5)} = \left(A_{xi}^{(5)}, A_{yi}^{(5)} \right)$ represents the mean-field advection:

$$\begin{cases} A_{xi}^{(5)} = \mathbf{v}_i^{(1)} \cdot \nabla_X \langle \mathbf{u}_i^{(2)} \rangle + \mathbf{v}_i^{(2)} \cdot \nabla_X \langle \mathbf{u}_i^{(1)} \rangle \\ A_{yi}^{(5)} = \mathbf{v}_i^{(1)} \cdot \nabla_X \langle \mathbf{v}_i^{(2)} \rangle + \mathbf{v}_i^{(2)} \cdot \nabla_X \langle \mathbf{v}_i^{(1)} \rangle. \end{cases} \quad (3.23)$$

Term $\mathbf{R}_i^{(5)} = (R_{xi}^{(5)}, R_{yi}^{(5)})$ represents the Reynolds stresses:

$$\begin{cases} R_{xi}^{(5)} = \langle \mathbf{v}_i^{\prime(2)} \cdot \nabla \mathbf{u}_i^{\prime(3)} \rangle + \langle \mathbf{v}_i^{\prime(3)} \cdot \nabla \mathbf{u}_i^{\prime(2)} \rangle \\ R_{yi}^{(5)} = \langle \mathbf{v}_i^{\prime(2)} \cdot \nabla \mathbf{v}_i^{\prime(3)} \rangle + \langle \mathbf{v}_i^{\prime(3)} \cdot \nabla \mathbf{v}_i^{\prime(2)} \rangle. \end{cases} \quad (3.24)$$

In the thickness equation, the roughness-induced eddy forcing appears first at $O(\varepsilon^7)$:

$$\begin{aligned} \frac{\partial \langle h_i^{(4)} \rangle}{\partial T} + \frac{\partial}{\partial X} \left(\sum_{j=1}^5 \langle \mathbf{u}_i^{(j)} \rangle \langle h_i^{(5-j)} \rangle + \langle \mathbf{u}_i^{\prime(2)} h_i^{\prime(3)} \rangle + \langle \mathbf{u}_i^{\prime(3)} h_i^{\prime(2)} \rangle \right) + \\ + \frac{\partial}{\partial Y} \left(\sum_{j=1}^5 \langle \mathbf{v}_i^{(j)} \rangle \langle h_i^{(5-j)} \rangle + \langle \mathbf{v}_i^{\prime(2)} h_i^{\prime(3)} \rangle + \langle \mathbf{v}_i^{\prime(3)} h_i^{\prime(2)} \rangle \right) = 0, \end{aligned} \quad (3.25)$$

where it is represented by terms $\langle \mathbf{v}_i^{\prime(2)} h_i^{\prime(3)} \rangle$ and $\langle \mathbf{v}_i^{\prime(3)} h_i^{\prime(2)} \rangle$. These eddy-transfer components are treated using the Transformed Eulerian Mean (TEM) framework (e.g., *Andrews and McIntyre, 1976*), which reformulates governing equations in terms of residual circulation. The result of this transformation is a system where small-scale forcing appears exclusively in the momentum equations, which leads to several conceptual and technical simplifications. In the present context, the residual velocities take the form

$$\mathbf{v}_{res\ i} = \langle \mathbf{v}_i^{(5)} \rangle + \frac{\langle \mathbf{v}_i^{\prime(2)} h_i^{\prime(3)} \rangle + \langle \mathbf{v}_i^{\prime(3)} h_i^{\prime(2)} \rangle}{h_i^{(0)}}. \quad (3.26)$$

We now use (3.26) to express the momentum equations (3.22) in terms of residual, rather than mean velocities:

$$\frac{\partial \langle \mathbf{v}_i^{(2)} \rangle}{\partial T} + \mathbf{A}_i^{(5)} + (-f_{v_{res\ i}}, f_{u_{res\ i}}) = -\nabla_X \langle p_i^{(3)} \rangle - \delta_{ni} \gamma_0 \frac{\langle \mathbf{v}_n^{(3)} \rangle}{h_n^{(0)}} + \mathbf{D}_i^{(5)}, \quad (3.27)$$

where $\mathbf{D}_i^{(5)} = (D_{xi}^{(5)}, D_{yi}^{(5)})$ represents small-scale momentum forcing:

$$\begin{cases} D_{xi}^{(5)} = -R_{xi}^{(5)} - q_i^{(0)} \langle \mathbf{v}_i^{\prime(2)} h_i^{\prime(3)} \rangle - q_i^{(0)} \langle \mathbf{v}_i^{\prime(3)} h_i^{\prime(2)} \rangle \\ D_{yi}^{(5)} = -R_{yi}^{(5)} + q_i^{(0)} \langle \mathbf{u}_i^{\prime(2)} h_i^{\prime(3)} \rangle + q_i^{(0)} \langle \mathbf{u}_i^{\prime(3)} h_i^{\prime(2)} \rangle. \end{cases} \quad (3.28)$$

These expressions can be further simplified by combining (3.24), (3.8), and (3.13):

$$\begin{cases} D_{xi}^{(5)} = h_i^{(0)} \langle \mathbf{v}_i^{\prime(2)} q_i^{\prime(3)} \rangle \\ D_{yi}^{(5)} = -h_i^{(0)} \langle \mathbf{u}_i^{(2)} q_i^{\prime(3)} \rangle. \end{cases} \quad (3.29)$$

To complete the development of the model, it is necessary to express the PV fluxes $\mathbf{R}_q = h_i^{(0)} \langle \mathbf{v}_i^{\prime(2)} q_i^{\prime(3)} \rangle$ in terms of large-scale properties. To that end, we turn to the fourth-order

potential vorticity equation (3.12). Following *Radko* (2024), we perform the analysis in the Fourier space and evaluate \mathbf{R}_q using the Parseval identity (2.16):

$$\langle \mathbf{v}_i^{(2)} q_i^{(3)} \rangle = \iint \tilde{\mathbf{v}}_i^{(2)} \cdot \text{conj}(\tilde{q}_i^{(3)}) dk dl. \quad (3.30)$$

Since the PV equation (3.12) provides only the along-flow variation in $q_i^{(3)}$, we adopt the flow-following coordinate system

$$\begin{cases} \hat{k} = k \cos \theta + l \sin \theta \\ \hat{l} = -k \sin \theta + l \cos \theta, \end{cases} \quad (3.31)$$

where the flow-orientation variable θ is defined by

$$\cos(\theta) = \frac{u_i^{(1)}}{|\mathbf{v}_i^{(1)}|}, \quad \sin(\theta) = \frac{v_i^{(1)}}{|\mathbf{v}_i^{(1)}|}. \quad (3.32)$$

In the flow-following coordinate system, the Fourier image of the left-hand side of (3.12) is $|\mathbf{v}_i^{(1)}| \hat{k} \tilde{q}_i^{(3)}$. The resulting explicit expression for $\tilde{q}_i^{(3)}$ is then used to evaluate (3.30) and thereby determine \mathbf{R}_q :

$$\begin{cases} h_i^{(0)} \langle u_i^{(2)} q_i^{(3)} \rangle = \frac{2\pi f^2}{V h_i^{(0)2}} \sin \theta \int \left(\nu_0 \kappa + \frac{\delta_{ni} \gamma_0}{h_i^{(0)} \kappa} \right) |h_i^{(2)}|^2 d\kappa \\ h_i^{(0)} \langle v_i^{(2)} q_i^{(3)} \rangle = -\frac{2\pi f^2}{V h_i^{(0)2}} \cos \theta \int \left(\nu_0 \kappa + \frac{\delta_{ni} \gamma_0}{h_i^{(0)} \kappa} \right) |h_i^{(2)}|^2 d\kappa. \end{cases} \quad (3.33)$$

The multiscale analysis is now complete, and we rewrite the evolutionary large-scale equations for the bottom layer using the original independent variables (x, y, t) in lieu of (X, Y, T) . The entire set of evolutionary large-scale equations is reconstructed by combining all (x, y) -averaged balances. The result is simplified by introducing the large-scale field variables

$$\bar{\mathbf{v}}_i = \sum_{j=1}^4 \varepsilon^j \langle \mathbf{v}_i^{(j)} \rangle + \varepsilon^5 \mathbf{v}_{res}, \quad \bar{h}_i = \sum_{j=0}^5 \varepsilon^j \langle h_i^{(j)} \rangle, \quad \bar{p}_i = \sum_{j=-1}^5 \varepsilon^j \langle p_i^{(j)} \rangle, \quad (3.34)$$

which leads to

$$\begin{cases} \frac{\partial \bar{\mathbf{v}}_i}{\partial t} + (\bar{\mathbf{v}}_i \cdot \nabla) \bar{\mathbf{v}}_i + (-f \bar{v}_i, f \bar{u}_i) = -\nabla \bar{p}_i + \nu \nabla^2 \bar{\mathbf{v}}_i - \delta_{ni} \gamma_b \frac{\bar{\mathbf{v}}_i}{h_i} + \delta_{li} \frac{\boldsymbol{\tau}}{h_i} + \mathbf{D}_i^{(fast)} \\ \frac{\partial \bar{h}_i}{\partial t} + \nabla \cdot (\bar{\mathbf{v}}_i \bar{h}_i) = 0, \end{cases} \quad (3.35)$$

where $\mathbf{D}_i^{(fast)}$ is the roughness-induced drag:

$$\mathbf{D}_i^{(fast)} = \varepsilon^5 \mathbf{D}_i^{(5)} = -\frac{2\pi f^2 \nu}{\bar{h}_i^2} \frac{\bar{\mathbf{v}}_i}{|\bar{\mathbf{v}}_i|^2} \int a_i^2 \left(\nu \kappa + \frac{\delta_{ni} \gamma}{h_i \kappa} \right) |\eta_s|^2 d\kappa. \quad (3.36)$$

In deriving (3.35), we have neglected $o(\varepsilon^5)$ terms in the momentum equations and $o(\varepsilon^7)$ terms in the thickness equation. Thus, the explicit viscous term $\nu \nabla^2 \mathbf{v}_i \sim O(\varepsilon^7)$ could have been neglected.

However, it is retained in (3.35) to maintain the structural similarity with the governing equations (2.4). Its inclusion does not affect the asymptotic accuracy of the large-scale model.

The expression (3.36) is analogous to the forcing patterns in the local model (*Radko, 2024*). The key difference is that the roughness signal is now distributed through the entire water column. This signal is modulated by the attenuation factors a_i , which can be readily obtained for a given stratification pattern (\bar{h}_i) using (3.19). It should be emphasized that the attenuation factors a_i become vanishingly small in the limit of $\bar{h}_i \rightarrow 0$. This feature has far-reaching consequences for implementing the sandpaper parameterization in numerical isopycnal models. In realistic configurations, density interfaces often intersect the seafloor, and the bottom layer depth in such locations approaches zero. The roughness-induced forcing in the local model increases without bound ($|\mathbf{D}_{loc}| \propto \bar{h}_n^{-2}$) for $\bar{h}_n \rightarrow 0$. In contrast, the non-local model remains well-behaved and physical. To highlight this property, we express the foregoing formulation in terms of the normalized attenuation factors $b_i = \frac{a_i}{\bar{h}_i}$, which reduces (3.36) to

$$\mathbf{D}_i^{(fast)} = -2\pi f^2 \frac{\bar{\mathbf{v}}_i}{|\bar{\mathbf{v}}_i|^2} \int b_i^2 \left(\nu \kappa + \frac{\delta_{ni} \gamma}{\bar{h}_i \kappa} \right) |\eta_s|^2 \kappa d\kappa. \quad (3.37)$$

The attenuation model (3.19) takes the form

$$\begin{cases} f^2 (b_i - b_{i+1}) + \kappa^2 B_{i,i+1} \sum_{j=1}^i \bar{h}_j b_j = 0, & i = 1, \dots, n-1 \\ \sum_{i=1}^n \bar{h}_i b_i = 1. \end{cases} \quad (3.38)$$

3.2. Regularization

The large-scale model in (3.35), (3.37), and (3.38) represents a closed system of evolutionary equations that captures flow forcing by rough topography. However, there is one physically suspicious and computationally inconvenient feature of this set—the singularity of the forcing term in the limit of weak velocities $|\bar{\mathbf{v}}_i| \rightarrow 0$. The origin of this singularity lies in the high Reynolds number assumption used in the large-scale model. To regularize the limit $|\bar{\mathbf{v}}_i| \rightarrow 0$, we consider a strongly dissipative system with $\text{Re} \ll 1$ and then develop a hybrid model that captures the transition between fast-flow and slow-flow models. The slow-flow model is described in Appendix A. The key result is the topographic forcing function $\mathbf{D}_i^{(slow)}$ that replaces $\mathbf{D}_i^{(fast)}$ in (3.35) for weak velocities:

$$\mathbf{D}_i^{(slow)} = -\delta_{ni} G^{(slow)} \bar{\mathbf{v}}_i, \quad (3.39)$$

where the expression for $G^{(slow)}$ in terms of seafloor properties is given in (A17). In contrast to the fast-flow model (3.37), the forcing function $\mathbf{D}_i^{(slow)}$ is well-behaved in the limit $|\bar{\mathbf{v}}_i| \rightarrow 0$, which makes it possible to regularize the sandpaper parameterization.

The algorithm used to bridge the fast-flow and slow-flow solutions follows the one adopted in *Radko (2024)*. The forcing functions are first written as

$$\mathbf{D}_i^{(slow)} = -\delta_{ni} G^{(slow)} |\bar{\mathbf{v}}_i| \mathbf{s}, \quad \mathbf{D}_i^{(fast)} = -G_i^{(fast)} |\bar{\mathbf{v}}_i|^{-1} \mathbf{s}, \quad (3.40)$$

where

$$G_i^{(fast)} = 2\pi f^2 \int b_i^2 \left(\nu \kappa + \frac{\delta_{ni} \gamma}{h_i \kappa} \right) |\eta_s|^2 \kappa d\kappa. \quad (3.41)$$

In (3.40), $\mathbf{s} \equiv \frac{\bar{\mathbf{v}}_i}{|\bar{\mathbf{v}}_i|}$ denotes the unit vector aligned with the flow, and the normalized attenuation factors (b_i) in (3.41) are computed from (3.38). Next, we introduce the analytical function $A_i(|\bar{\mathbf{v}}_i|)$ that converges to $\delta_{ni} G^{(slow)} |\bar{\mathbf{v}}_i|$ and $G_i^{(fast)} |\bar{\mathbf{v}}_i|^{-1}$ in the slow-flow and fast-flow limits, respectively. For the bottom layer, we use

$$A_n = \sqrt{G^{(slow)} G_n^{(fast)}} \exp\left(-\sqrt{1 + \ln^2(|\bar{\mathbf{v}}_n| V_{Cn}^{-1})}\right). \quad (3.42)$$

The critical velocity $V_{Cn} = \sqrt{\frac{G_n^{(fast)}}{G^{(slow)}}}$ in (3.42) represents the transition point between fast-flow and slow-flow regimes. For upper layers ($i = 1, \dots, n-1$), we consider

$$A_i = \tanh^4(|\bar{\mathbf{v}}_i| V_{Ci}^{-1}) G_i^{(fast)} |\bar{\mathbf{v}}_i|^{-1}, \quad (3.43)$$

where $V_{Ci} = \sqrt{\frac{G_0^{(fast)}}{G^{(slow)}}}$ and $G_0^{(fast)} = 2\pi \frac{f^2}{h_n^2} \int \left(\nu \kappa + \frac{\gamma}{h_n \kappa} \right) |\eta_s|^2 d\kappa$. Function (3.43) converges to $G_i^{(fast)} |\bar{\mathbf{v}}_i|^{-1}$ for $|\bar{\mathbf{v}}_i| \gg V_{Ci}$ but becomes vanishingly small, on the order of $O(|\bar{\mathbf{v}}_i|^3)$, for $|\bar{\mathbf{v}}_i| \ll V_{Ci}$. Both properties conform to the anticipated patterns of the roughness-induced drag in the fast-flow (Sec. 3.1) and slow-flow (Appendix A) limits. The hybrid model of topographic forcing becomes

$$\mathbf{D}_i^{(hybrid)} = -A_i \frac{\bar{\mathbf{v}}_i}{V_{Ci}}. \quad (3.44)$$

The corresponding evolutionary large-scale equations based on the hybrid model are obtained by replacing $\mathbf{D}_i^{(fast)}$ in (3.35) by $\mathbf{D}_i^{(hybrid)}$. In dimensional units, the resulting system takes the form

$$\begin{cases} \frac{\partial \bar{\mathbf{v}}_i^*}{\partial t^*} + (\bar{\mathbf{v}}_i^* \cdot \nabla) \bar{\mathbf{v}}_i^* + (-f^* \bar{\mathbf{v}}_i^*, f^* \bar{u}_i^*) = -\frac{1}{\rho_0^*} \nabla \bar{p}_i^* + \nu^* \nabla^2 \bar{\mathbf{v}}_i^* - \delta_{ni} \gamma^* \frac{\bar{\mathbf{v}}_i^*}{h_i^*} + \delta_{1i} \frac{\boldsymbol{\tau}^*}{\rho_0^* h_i^*} + \mathbf{D}_i^{(hybrid)} \\ \frac{\partial \bar{h}_i^*}{\partial t^*} + \nabla \cdot (\bar{\mathbf{v}}_i^* \bar{h}_i^*) = 0, \end{cases} \quad (3.45)$$

where $\mathbf{D}_i^{(hybrid)} = L^* f_0^{*2} \mathbf{D}_i^{(hybrid)}$. This hybrid formulation is well-behaved regardless of the flow speed and can be readily implemented in parametric simulations.

4. Implementation and testing

4.1. Experimental Configuration

To assess the performance of the sandpaper model, we turn to simulations performed using HYCOM. The roughness-resolving experiments are compared with solutions based on the parameterized system. To streamline the interpretation, the entire analysis is carried out in

dimensional units. The asterisks, which previously denoted dimensional quantities, will not be used hereafter.

The following system is designed to represent the dynamics of the abyssal ocean, directly affected by seafloor roughness. The reference ocean depth is set to $H_0 = 10^3$ m, and the reduced gravity is assigned a value of $g' \equiv g \frac{\rho_n - \rho_1}{\rho_0} = 10^{-3} \text{ ms}^{-2}$, which is representative of deep ocean regions. We also assume that the density differences between adjacent layers are identical: $\rho_{i+1} - \rho_i = \frac{\rho_n - \rho_1}{n-1}$. The calculations are performed on the f -plane with $f = 10^{-4} \text{ s}^{-1}$ and the dissipation parameters are $\nu = 10 \text{ m}^2 \text{ s}^{-1}$ and $\gamma = 0$. We configure HYCOM with ten layers of background thickness of 100 m each.

The non-local model is tested on the canonical vortex spin-down problem. We consider an initially barotropic Gaussian vortex

$$\psi = C \exp\left(-\frac{r^2}{R^2}\right), \quad r = \sqrt{x^2 + y^2}, \quad (4.1)$$

where ψ is the streamfunction associated with the velocity field $(u_i, v_i) = \left(-\frac{\partial\psi}{\partial y}, \frac{\partial\psi}{\partial x}\right)$, and

$R = 5 \times 10^4 \text{ m}$ is an effective radius. The amplitude $C = 5 \times 10^3 \text{ m}^2 \text{ s}^{-1}$ used in simulations corresponds to the maximal radial velocity of $V_{\max} = 0.086 \text{ ms}^{-1}$. We assume doubly periodic lateral boundary conditions and employ a relatively wide computational domain of size $(L_x, L_y) = (4 \cdot 10^5 \text{ m}, 4 \cdot 10^5 \text{ m})$, which minimizes the influence of boundaries on the vortex dynamics. The roughness-resolving simulations employ a fine mesh with $(N_x, N_y) = (512, 512)$ grid points. The parametric simulations are largely insensitive to resolution, and in the following examples we use $(N_x, N_y) = (256, 256)$.

Topography is represented by irregular small-scale variability based on the observationally derived spectrum of *Goff and Jordan* (1988):

$$P_{GJ} = \frac{\mu - 2}{(2\pi)^3} \left(\frac{\eta_{GJ}}{k_0 l_0}\right)^2 \left(1 + \left(\frac{k}{2\pi k_0}\right)^2 + \left(\frac{l}{2\pi l_0}\right)^2\right)^{-\mu/2}, \quad (4.2)$$

where η_{GJ} is an adjustable coefficient that allows us to specify the desired magnitude of roughness. Following *Nikurashin et al.* (2014), we consider

$$\mu = 3.5, \quad k_0 = l_0 = 1.8 \times 10^{-4} \text{ m}^{-1}. \quad (4.3)$$

The small-scale topography in physical space (η_s) is obtained as a sum of Fourier modes with random phases and spectral amplitudes conforming to (4.2). The wavelengths of these modes are constrained from above and below:

$$L_{\min} < \frac{2\pi}{\kappa} < L_{\max}. \quad (4.4)$$

We assume $L_{\max} = 3 \times 10^4 \text{ m}$ to satisfy (2.9) and $L_{\min} = 3 \times 10^3 \text{ m}$ to ensure that all topographic scales are well resolved. The spectrum is normalized so that the root-mean-square small-scale depth variation is $\eta_{rms} = 15 \text{ m}$.

Two sets of simulations are presented. The first set considers flat large-scale bathymetry and will be referred to as *FLAT* hereafter. The total depth is given by

$$FLAT: \quad H = H_0 - \eta_s(x, y), \quad (4.5)$$

which is used to explore isopycnal surfaces that do not intersect with rough topography. Therefore, the *FLAT* simulations enable us to assess the merits of local and non-local parameterizations. The second set takes into account large-scale depth variability and will be denoted as *BOWL*, reflecting the bowl-shaped domain (Fig. 2) used in these simulations. The depth pattern is given by

$$BOWL: \quad H = H_0 - ar^2 - \eta_s(x, y), \quad (4.6)$$

where $a = \frac{50}{R^2} = 2 \times 10^{-8} \text{ m}^{-1}$, and r is the distance from the domain center. In these experiments, the isopycnals intersect with the topography, and layers vanish ($\bar{h}_i \rightarrow 0$) in some locations, which cannot be treated with the local model. The analysis of both *FLAT* and *BOWL* simulation sets is focused on comparing non-local parametric and roughness-resolving simulations.

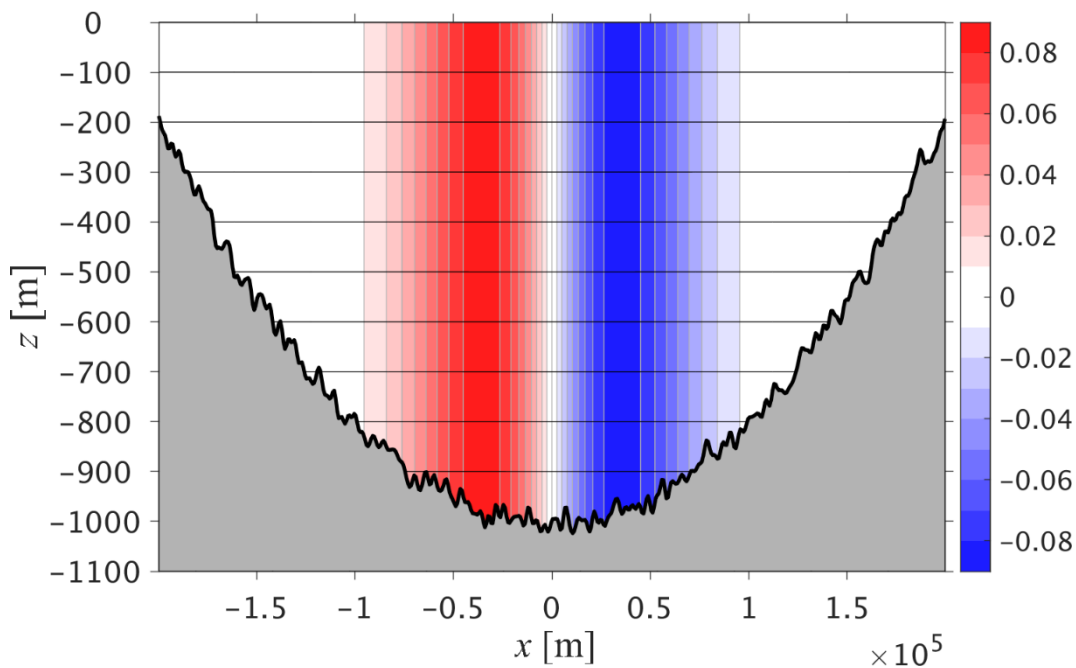


Figure 2. The zonal section across the center of the computational domain used in the roughness-resolving *BOWL* experiments. The horizontal lines indicate the density interfaces, which often intersect bathymetry. The red-blue pattern represents the initial meridional velocity $v_i [m s^{-1}]$ associated with the Gaussian streamfunction (4.1).

4.2. FLAT simulations

Fig. 3 presents the thickness h_i and absolute velocity $|\mathbf{v}_i|$ in layers $i = 8, 9$, and 10 realized at $t = 10$ days in the roughness-resolving FLAT simulation. These patterns reflect the presence of small-scale flow components in deep layers. Their intensity, however, rapidly decreases away from the seafloor. This tendency is consistent with the estimate of vertical attenuation of roughness-induced perturbations in Radko (2022b). The suggested effective scale of the region directly affected by roughness is $h_{\text{eff}} \sim \frac{f}{N\kappa_s}$, where $N \sim \sqrt{\frac{g'}{H_0}}$ is the buoyancy frequency and κ_s is the representative wavenumber of small-scale topography. For the present configuration, $h_{\text{eff}} \sim 100$ m, which explains the attenuation pattern in Fig. 3. In layers $i \geq 7$, the small-scale signal is weak and largely inconsequential.

To examine the temporal pattern of the vortex spin-down, Fig. 4 presents the time series of the net spatially averaged large-scale kinetic energy $\bar{E}_{\text{tot}}(t) = \frac{1}{2} \langle \bar{u}^2 + \bar{v}^2 \rangle_{x,y,z}$. In each layer, the large-scale velocity components (\bar{u}_i, \bar{v}_i) are computed by retaining harmonics of (u_i, v_i) with wavelengths exceeding the roughness scales ($2\pi/\kappa > L_{\text{max}}$). These are the flow components that the sandpaper theory is designed to represent. Therefore, the diagnostics in Fig. 4 permit direct comparison of roughness-resolving and parametric simulations.

The kinetic energy in the roughness-resolving HYCOM simulation, indicated by the solid black curve in Fig. 4, monotonically decreases in time, and the spin-down is effectively completed by $t = 250$ days. The analogous parametric simulation is performed using the non-local sandpaper model (3.45), in which the attenuation factors are computed using (3.38). The record of $\bar{E}_{\text{tot}}(t)$ in the parametric model (solid red curve in Fig. 4) closely follows the roughness-resolving calculation. The non-local sandpaper theory underestimates the vortex energy throughout the entire simulation, but the differences are small ($\Delta E < 1.7 \times 10^{-8} \text{ m}^2 \text{ s}^{-2}$).

It is interesting to place these results in the context of the relative benefits of local and non-local formulations. Therefore, we also present the simulation performed using the local sandpaper model (solid blue curve). The numerical algorithm is modified by assigning the attenuation factors values of $a_i = \delta_{ni}$ that define the local formulation. Fig. 4 indicates that the local model substantially overestimates the vortex decay rate. Its poor performance in the present configuration is not surprising. The local model assumes from the outset that the roughness-induced perturbations are fully contained in the bottom layer, which demands that $h_{\text{eff}} \ll h_n$. However, at present, we use a relatively fine vertical discretization with $h_{\text{eff}} \sim h_n$, violating the very assumption of the perturbation locality.

16

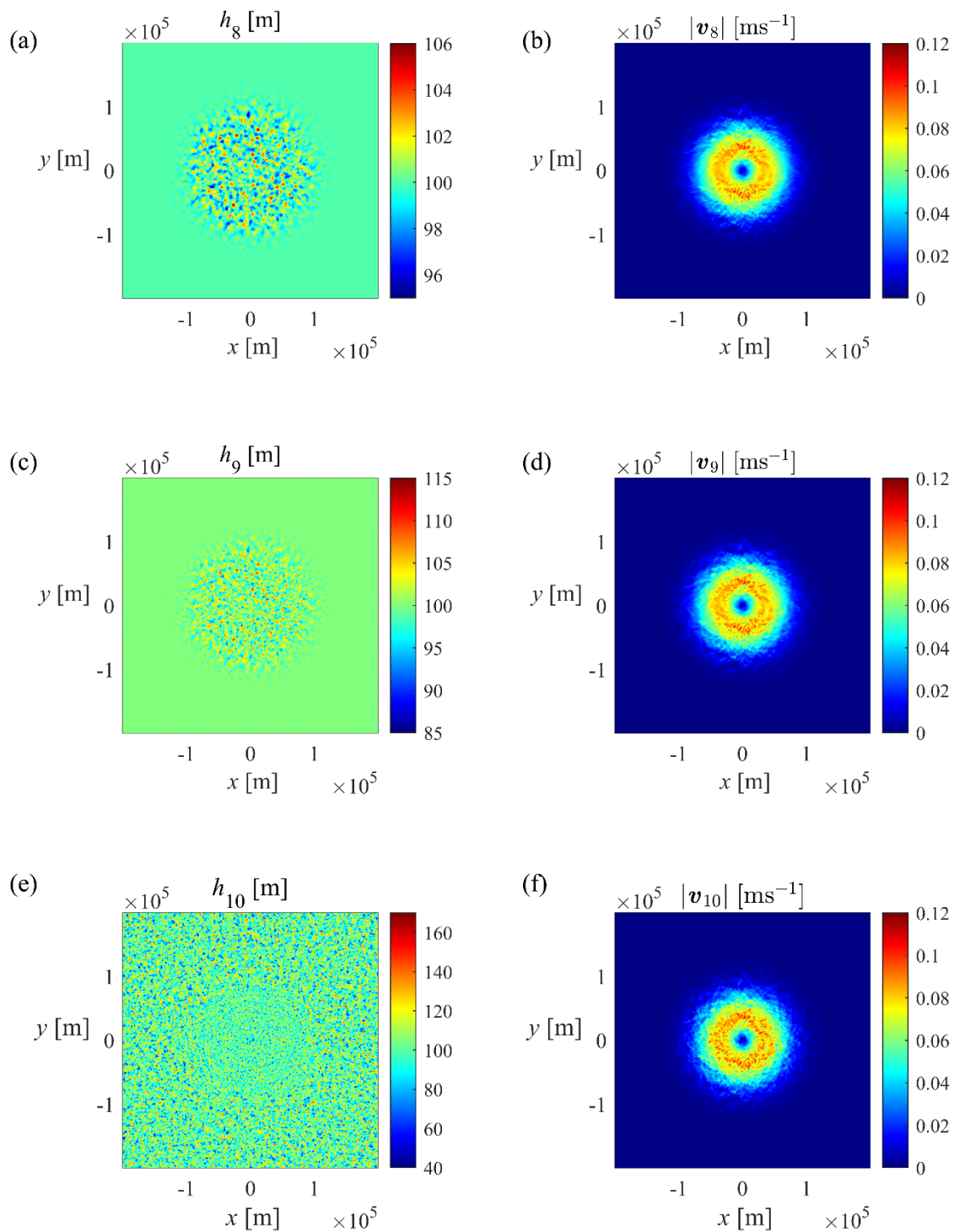


Figure 3. The roughness-resolving HYCOM simulation in the *FLAT* category. The instantaneous patterns of the layer thicknesses (left panels) and absolute velocities (right panels) are shown for $t = 10$ days. Panels (a,b), (c,d), and (e,f) represent layers 8, 9, and 10, respectively.

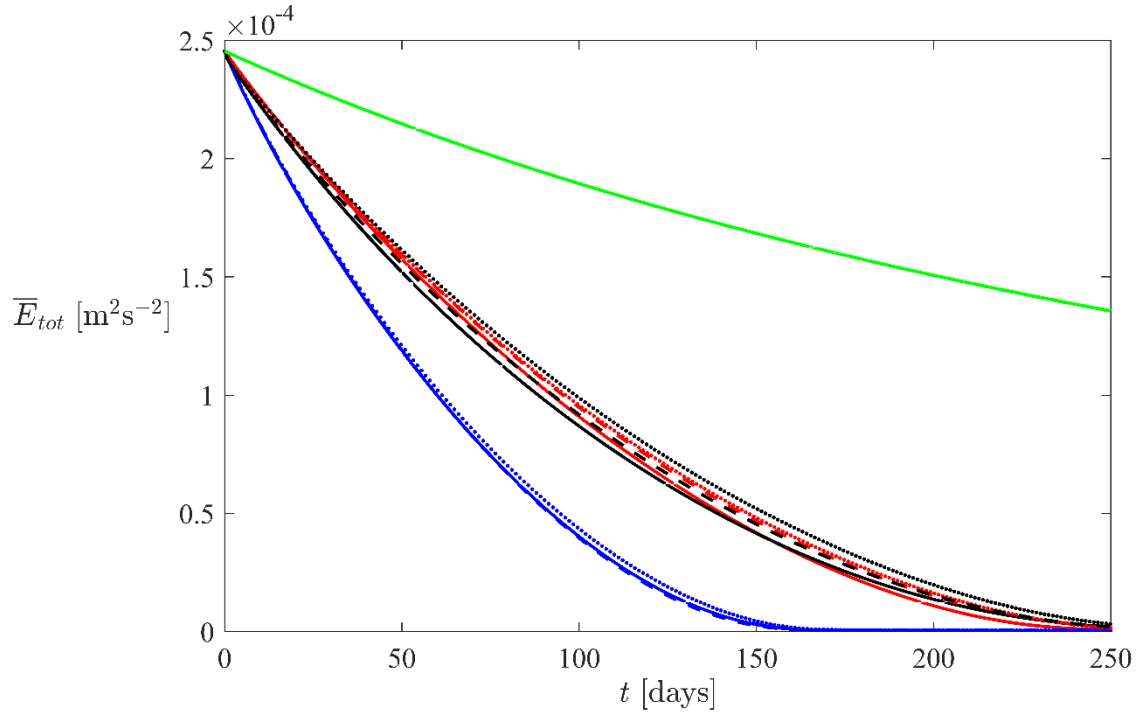


Figure 4. The time series of the mean domain-integrated large-scale kinetic energy \bar{E}_{tot} for simulations in the *FLAT* category. The roughness-resolving, non-local parametric, and local parametric simulations are indicated by black, red, and blue curves, respectively. Solid curves represent HYCOM-based simulations. Also included are the results of the quasi-geostrophic (dotted curves) and shallow-water (dashed curves) spectral simulations. The overlapping green curves represent smooth-topography ($\eta_s = 0$) simulations.

To ensure that the results in Fig. 4 are not model-dependent, we have reproduced the *FLAT* HYCOM simulations using the Fourier-based spectral dealiased model employed in our previous studies. Two versions of the spectral model have been considered. The first model (dashed curves in Fig. 4) integrates the shallow-water equations and their parametric counterparts (Radko, 2024). The second spectral model (Radko, 2023a) is based on the quasi-geostrophic framework (e.g., Pedlosky, 1987) and is indicated by dotted curves. Since the algorithms in all models differ substantially, their close agreement lends further credence to our findings.

In this regard, we wish to highlight the consistency of shallow-water and quasi-geostrophic simulations. It yields insight into the role of fully nonlinear processes associated with finite-amplitude thickness variation and ageostrophic velocities, which are treated as higher-order corrections in the quasi-geostrophic model. Of particular concern is the assumption of weak variation in layer thickness, which is at odds with the pattern of h_{10} in our configuration (Fig. 3). Thus, the agreement of quasi-geostrophic and shallow-water models implies that fully nonlinear processes, not captured by the quasi-geostrophic model, have a limited impact on roughness-induced bottom drag. We find this result to be rather uplifting, given the considerable conceptual insights and computational gains brought by the quasi-geostrophic approximation.

Overall, the diagnostics in Fig. 4 reinforce our belief that seafloor roughness can substantially impact the evolution of large-scale oceanic flows (LaCasce *et al.*, 2019; Radko, 2023a,b). This point is illustrated by presenting the smooth-bottom ($\eta_s = 0$) simulation. The vortex evolution in this experiment is qualitatively dissimilar to its rough-bottom counterpart, and the decay rates differ by a factor of three. It should also be noted that the roughness level considered in this study is

relatively low ($\eta_{rms} = 15$ m). The small-scale variability in many regions of the World Ocean is much more pronounced, with $\eta_{rms} > 300$ m not uncommon (Goff, 2020). Yet, even the present, relatively mild roughness dramatically accelerates spin-down.

4.3. BOWL simulations

One of the motivating factors for developing the non-local parameterization was the requirement for the model to perform well even near the intersections of isopycnals with topography. Since the bottom layer depth in such locations approaches zero, the local parametrization there is inapplicable. The question arises of how accurate the non-local parametrization might be in such challenging conditions. To that end, we use the computational domain shown in Fig. 2, where density interfaces intersect with bathymetry at several locations. The spectral models (Sec. 4.2) are not designed to treat systems where density interfaces intersect with topography, and therefore, we present only HYCOM-based simulations.

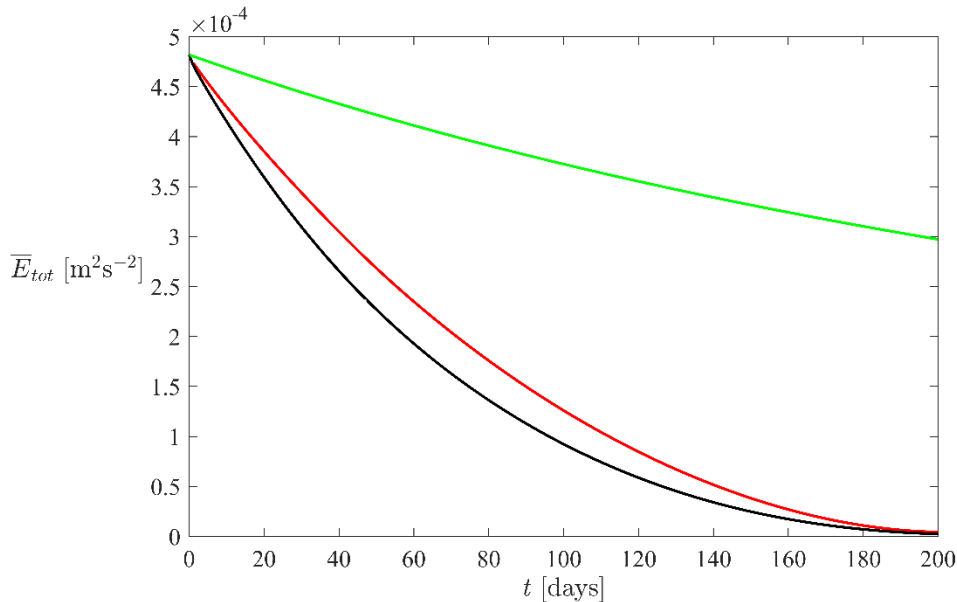


Figure 5. The time series of mean domain-integrated large-scale kinetic energy \bar{E}_{tot} in the *BOWL* simulations. The roughness-resolving and non-local parametric simulations are indicated by black and red curves, respectively. The green curve represents the smooth-topography ($\eta_s = 0$) simulation.

Aside from different bathymetry, the design of *BOWL* simulations follows their *FLAT* counterparts. The temporal record of the total energy is presented in Fig. 5. As expected, the attempt to use the local parameterization has led to the catastrophic failure of the simulation. Therefore, Fig. 5 presents the roughness-resolving simulation (back curve) and the non-local parameterization (red). The parametric and roughness-resolving $\bar{E}_{tot}(t)$ patterns are generally consistent, albeit the sandpaper theory tends to overestimate the energy.

While the diagnostics in Fig. 5 focused on the integral properties of the system, we also find it instructive to examine the evolutionary patterns of individual layers. Particularly interesting are the dynamics of the tenth layer. It is located immediately above rough topography, and its thickness gradually reduces from the maximal value at the vortex center to zero at $r \approx 7 \times 10^4$ m. These features make the tenth layer particularly vulnerable to the roughness-induced forcing. We also

expect that the non-local processes, which preferentially affect relatively thin layers near the seafloor, should impact the tenth layer more than all others. Therefore, we present (Fig. 6) the time series of the mean large-scale kinetic energy in the tenth layer (\bar{E}_{10}). Fig. 6 suggests that the roughness-resolving and non-local parametric patterns of $\bar{E}_{10}(t)$ are generally consistent, although the sandpaper theory tends to underestimate the vortex spin-down rate.

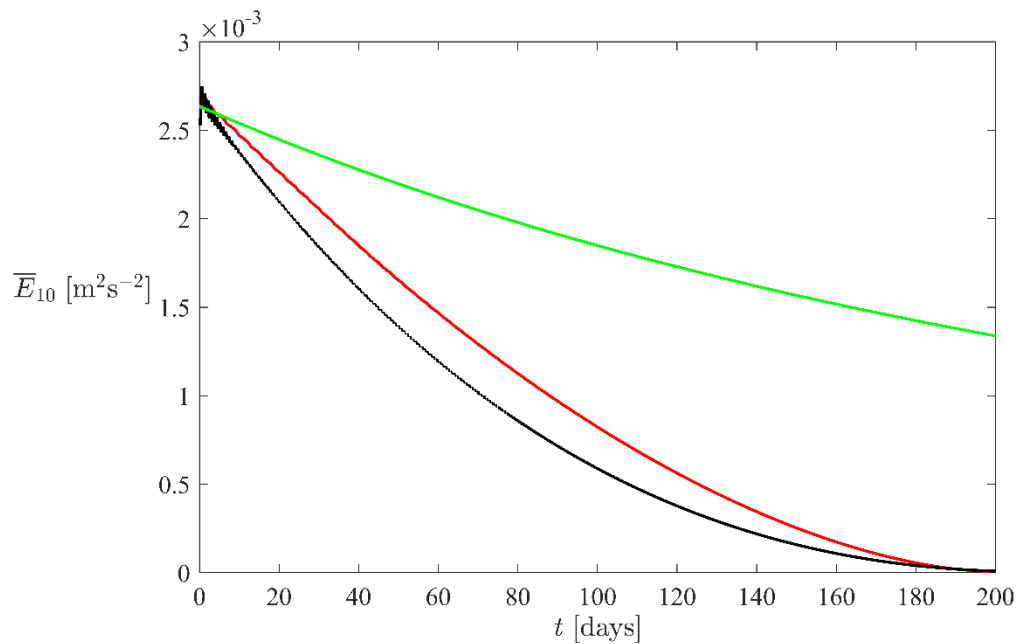


Figure 6. The same as in Fig. 5, but for the mean large-scale kinetic energy in the tenth layer (\bar{E}_{10}).

5. Discussion

Rough topography of the ocean basins presents a major challenge for theoretical analyses of circulation, numerical modeling, and the interpretation of field measurements. The cumulative impact of kilometer-scale topographic features on much broader flow patterns can be dramatic (*LaCasce et al., 2019; Radko, 2020*) and lead, in some cases, to unexpected consequences (e.g., *Gulliver and Radko, 2022*). Yet, these small-scale seafloor patterns are unresolved by global climate and operational predictive systems, and our ability to concisely represent the effects of roughness remains limited. Empirical drag laws currently used by general circulation models do not capture the dynamics of roughness-induced forcing, motivating efforts to design more targeted closure schemes.

Our previous attempts to formulate physics-based parameterizations of roughness have led to the development of the so-called sandpaper model (*Radko, 2024*). This model is based on the asymptotic analysis of governing shallow-water equations. Therefore, unlike many other closures, it does not rely on empirical assumptions and does not contain adjustable parameters. Another appealing feature of this approach is that it circumvents the requirement to consider specific patterns of small-scale topography, which vary from one location to the other. Instead, it focuses on the statistical spectrum of bathymetry, which holds promise of a more universal description of roughness-induced forcing.

The key shortcoming of these early efforts is the locality assumption. The lowest isopycnal layer was assumed to be deep enough to contain the entire region of the direct influence of roughness.

This assumption can be violated when the vertical resolution in the abyssal ocean is systematically increased (see the schematic in Fig. 1). Limitations of the local formulation become particularly apparent in the context of operational ocean simulations that use primarily isopycnic coordinates such as the Navy Global Ocean Forecast System (*Metzger et al.*, 2014), which is currently based on HYCOM. In these realistic configurations, density interfaces frequently intersect bathymetry, and the roughness-induced drag predicted by the local model becomes singular. It unphysically increases without bound, precluding the implementation of the sandpaper closure in its original form.

To overcome the deficiencies of the local closure, we develop the next-generation sandpaper model, which considers small-scale variability in the velocity and thickness in layers that are not in direct contact with the seafloor. The non-local processes are dynamically analogous to—but weaker than—the forcing mechanisms previously identified in the lowest layer by the local model. In the non-local model, the interaction of primary flows with rough terrain introduces small-scale variability throughout the water column. These topographically induced eddies, in turn, affect large-scale circulation patterns through the combination of the eddy form drag and Reynolds stresses. The non-local formulation is implemented in HYCOM, one of the mainstream general circulation models, which is expected to facilitate the adoption of sandpaper closure by the modeling community. The theory-based parameterization is tested on the canonical vortex spin-down problem and shown to be consistently more accurate than its local counterpart. The computational overhead of incorporating the non-local closure in HYCOM is minor and can be tolerated for most intents and purposes.

Besides the pragmatic interest in improving the fidelity of numerical forecasts, the non-local model may lead to further theoretical advancements. Of particular interest is the extension of the sandpaper formalism to continuously stratified systems. One of the pathways for the development of a fully three-dimensional z -coordinate sandpaper model is the analysis of the asymptotic thin-layer limit $\Delta\rho = \max_{1 \leq i \leq n-1} \{\rho_{i+1} - \rho_i\} \rightarrow 0$. This regime would have been inaccessible through its local formulation, which *a priori* assumes a sufficiently deep bottom layer. However, the non-local theory effectively removes the restriction on vertical discretization, making the model more flexible and broadening the range of potential applications. In addition to continuously stratified formulations, there are several other enhancements and extensions of the sandpaper model on our wish list. They include, but are not limited to, non-hydrostatic effects, non-isotropic bathymetric spectra, roughness-induced water mass transformation, and more precise interactive models of explicit dissipation.

Funding. Support of the National Science Foundation (grants OCE 2241625 and 2241626) and the Office of Naval Research (grant O2502017017085061) is gratefully acknowledged.

Declaration of Interests. The authors report no conflict of interest.

Appendix A. The slow-flow model

To identify the essential dynamics of flow-topography interaction of low Reynolds number flows, we consider the asymptotic sector $U = O(\varepsilon^2)$ and $v = O(\varepsilon)$, which corresponds to

$\text{Re} = \frac{LU^*}{\nu^*} = O(\varepsilon)$. The solutions obtained in this sector will be referred to as the slow-flow model.

The temporal variability is still represented by (3.1), albeit in this low-Re regime it is expected to be controlled by dissipative processes rather than by mean-field advection.

The frictional parameters and small-scale bathymetric variability are rescaled as follows:

$$v = \varepsilon v_0, \quad \gamma = \varepsilon \gamma_0, \quad \eta_s = \varepsilon^2 \eta_{s0}. \quad (\text{A1})$$

We seek the solution in terms of the following power series for velocity

$$\mathbf{v}_i = \varepsilon^2 \mathbf{v}_i^{(2)}(X, Y, T) + \sum_{j=3}^{\infty} \varepsilon^j \mathbf{v}_i^{(j)}(X, Y, x, y, T), \quad (\text{A2})$$

and pressure

$$p_i = p_i^{(0)}(X, Y, T) + \varepsilon p_i^{(1)}(X, Y, T) + \varepsilon^2 p_i^{(2)}(X, Y, T) + \sum_{j=3}^{\infty} \varepsilon^j p_i^{(j)}(X, Y, x, y, T). \quad (\text{A3})$$

The layer thicknesses are still represented by (3.6).

Following the approach used in Sec. 3, we first compute the leading-order perturbation balances. For the momentum equations, it is realized at $O(\varepsilon^3)$:

$$\begin{cases} f v_i^{(3)} = \frac{\partial p_i^{(3)}}{\partial x} \\ f u_i^{(3)} = -\frac{\partial p_i^{(3)}}{\partial y}. \end{cases} \quad (\text{A4})$$

The key insights into dynamics are brought by the small-scale $O(\varepsilon^4)$ balance of the PV equation (2.7):

$$u_i^{(2)} \frac{\partial q_i^{(2)}}{\partial x} + v_i^{(2)} \frac{\partial q_i^{(2)}}{\partial y} = \frac{v_0}{h_i^{(0)}} \nabla^2 \zeta_i^{(2)} - \frac{\gamma_0}{h_i^{(0)2}} \zeta_i^{(2)}, \quad (\text{A5})$$

where

$$q_i^{(2)} = -\frac{f h_i^{(2)}}{(h_i^{(0)})^2}. \quad (\text{A6})$$

The leading order small-scale component of the recursive relation (2.6) takes the form

$$B_{i,i+1} \sum_{j=1}^i h_j^{(2)} = 0, \quad i = 1, \dots, n-1, \quad (\text{A7})$$

and when it is combined with (3.18), we conclude that

$$h_i^{(2)} = -\delta_{ni} \eta_{s0}. \quad (\text{A8})$$

This result underscores the fundamental difference between the effects of roughness in fast and slow flows. While the vertical attenuation factor (a_i) in the fast-flow model attained finite values in several layers, the reduction in the flow speed for the same stratification pattern ($B_{i,i+1}$) has led to the localization of a roughness signal to the lowest layer: $a_i = \delta_{ni}$. In retrospect, this conclusion appears to be very natural and physical. The vertical transmission of the roughness signal is undoubtedly controlled by the flow speed. In the limiting case of a quiescent system, one expects a complete flattening of density interfaces. In this regime, (A4)–(A6) can be solved for small-scale velocity components as a function of roughness. The calculation is performed in the Fourier space and results in:

$$\begin{cases} \tilde{u}_n^{(3)} = \frac{fl(ku_n^{(2)} + lv_n^{(2)})}{(h_n^{(0)}\nu_0\kappa^2 + \gamma_0)\kappa^2} \tilde{\eta}_{s0} \\ \tilde{v}_n^{(3)} = -\frac{fk(ku_n^{(2)} + lv_n^{(2)})}{(h_n^{(0)}\nu_0\kappa^2 + \gamma_0)\kappa^2} \tilde{\eta}_{s0}. \end{cases} \quad (\text{A9})$$

and $\tilde{v}_i^{(3)} = 0$ for $i < n$.

The evolutionary large-scale system is obtained using the $O(\varepsilon^5)$ mean momentum equations:

$$\frac{\partial \mathbf{v}_i^{(2)}}{\partial T} + \left(-f \langle \mathbf{v}_i^{(5)} \rangle, f \langle u_i^{(5)} \rangle \right) = -\nabla_x \langle p_i^{(3)} \rangle - \delta_{ni} \gamma_{b0} \frac{\langle \mathbf{v}_n^{(4)} \rangle}{h_n^{(0)}}, \quad (\text{A10})$$

and $O(\varepsilon^7)$ thickness equation:

$$\frac{\partial \langle h_i^{(3)} \rangle}{\partial T} + \frac{\partial}{\partial X} \left(\sum_{j=2}^5 \langle u_i^{(j)} \rangle \langle h_i^{(5-j)} \rangle + \langle u_i^{(3)} h_i^{(2)} \rangle \right) + \frac{\partial}{\partial Y} \left(\sum_{j=2}^5 \langle v_i^{(j)} \rangle \langle h_i^{(5-j)} \rangle + \langle v_i^{(3)} h_i^{(2)} \rangle \right) = 0. \quad (\text{A11})$$

The large-scale forcing by the small-scale eddies is now represented by terms $\langle u_i^{(3)} h_i^{(2)} \rangle$ and $\langle v_i^{(3)} h_i^{(2)} \rangle$ in the thickness equation (A11). It is interesting that while the Reynolds stresses played a major role in the fast-flow model, now they are conspicuously missing in the momentum equations. Importantly, the roughness-induced forcing at this order is active only in the bottom layer ($i = n$).

Following the approach adopted for the fast-flow model, we incorporate the eddy transfer of thickness components into the residual-mean velocities (*Andrews and McIntyre, 1976*):

$$\mathbf{v}_{res\ i} = \langle \mathbf{v}_i^{(5)} \rangle + \frac{\langle \mathbf{v}_i^{(3)} h_i^{(2)} \rangle}{h_i^{(0)}}. \quad (\text{A12})$$

The eddy transfer terms are linked to the large-scale flow properties by combining (A8) with (A9) and applying the Parseval identity (2.16):

$$\begin{cases} \langle u_n^{(3)} h_n^{(2)} \rangle = -\pi v_n^{(2)} f \int \frac{|\tilde{\eta}_{s0}|^2 \kappa}{h_n^{(0)} \nu_0 \kappa^2 + \gamma} d\kappa \\ \langle v_n^{(3)} h_n^{(2)} \rangle = \pi u_n^{(2)} f \int \frac{|\tilde{\eta}_{s0}|^2 \kappa}{h_n^{(0)} \nu_0 \kappa^2 + \gamma} d\kappa. \end{cases} \quad (\text{A13})$$

Finally, we obtain the evolutionary large-scale equations by (i) introducing the following large-scale field variables:

$$\bar{\mathbf{v}}_i = \sum_{j=2}^4 \varepsilon^j \langle \mathbf{v}_i^{(j)} \rangle + \varepsilon^5 \mathbf{v}_{res\ i}, \quad \bar{h}_i = \sum_{j=0}^5 \varepsilon^j \langle h_i^{(j)} \rangle, \quad \bar{p}_i = \sum_{j=1}^5 \varepsilon^j \langle p_i^{(j)} \rangle, \quad (\text{A14})$$

(ii) combining all (x, y) -averaged balances, and (iii) reverting to the original independent variables (x, y, t) . The resulting system takes the form

$$\begin{cases} \frac{\partial \bar{\mathbf{v}}_i}{\partial t} + (-f\bar{\mathbf{v}}_i, f\bar{\mathbf{u}}_i) = -\nabla \bar{p}_i - \delta_{ni} \gamma_b \frac{\bar{\mathbf{v}}_i}{h_i} + \delta_{1i} \frac{\boldsymbol{\tau}}{h_i} + \delta_{ni} \mathbf{D}_n^{(slow)} \\ \frac{\partial \bar{h}_i}{\partial t} + \nabla \cdot (\bar{\mathbf{v}}_i \bar{h}_i) = 0. \end{cases} \quad (\text{A15})$$

The roughness-induced forcing $\mathbf{D}_n^{(slow)}$ in (A15) can be expressed as

$$\mathbf{D}_n^{(slow)} = -G^{(slow)} \bar{\mathbf{v}}_n, \quad (\text{A16})$$

where

$$G^{(slow)} = \frac{\pi f^2}{\bar{h}_n} \int \frac{|\tilde{\eta}_s|^2 \kappa}{\bar{h}_n \nu \kappa^2 + \gamma} d\kappa. \quad (\text{A17})$$

The forcing term (A16) represent the so-called form drag, which is caused by the pressure differences between the upstream and downstream sides of topographic features:

$$\mathbf{D}_n^{(slow)} \approx \frac{1}{\bar{h}_n} \langle \nabla \bar{p}_n \eta_s \rangle = -\frac{1}{\bar{h}_n} \langle \bar{p}_n \nabla \eta_s \rangle. \quad (\text{A18})$$

This forcing mechanism is fundamentally dissimilar to the one that controls the evolution of fast flows (Sec. 3.1)—the latter also relies on Reynolds stresses associated with roughness-generated eddies. For implementation in comprehensive models, it may be prudent to introduce the following correction to the slow-flow model (A17):

$$\bar{h}_n \rightarrow \bar{h}_n + rms(\eta_s), \quad (\text{A19})$$

which precludes the model's singularity at locations where concurrently $\bar{h}_n \rightarrow 0$ and $|\bar{\mathbf{v}}_n| \rightarrow 0$. Since the theoretical model from the outset assumes $(\bar{h}_n, \eta_s) \sim (1, \varepsilon^2)$, approximation (A19) does not affect the asymptotic accuracy of the solution.

REFERENCES

- ANDREWS, D. G., AND M. E. MCINTYRE, 1976: Planetary waves in horizontal and vertical shear: The generalized Eliassen-Palm relation and the mean zonal acceleration. *J. Atmos. Sci.*, **33**, 2031–2048.
- BLECK, R., 2002: An oceanic general circulation model framed in hybrid isopycnic-cartesian coordinates. *Ocean Modell.*, **4**, 55–88.
- CHASSIGNET, E. P., L. T. SMITH, G. R. HALLIWELL, AND R. BLECK, 2003. North Atlantic simulations with the HYbrid Coordinate Ocean Model (HYCOM): Impact of the vertical coordinate choice, reference density, and thermobaricity. *J. Phys. Oceanogr.*, **33**, 2504–2526.
- CHASSIGNET, E. P., H. E. HURLBURT, O. M. SMEDSTAD, G. R. HALLIWELL, A. J. WALLCRAFT, E. J. METZGER, B. O. BLANTON, C. LOZANO, D. B. RAO, P. J. HOGAN, AND A. SRINIVASAN, 2006. Generalized vertical coordinates for eddy-resolving global and coastal ocean forecasts. *Oceanography*, **19**(1), 20–31.
- CHASSIGNET, E. P., H. E. HURLBURT, E. J. METZGER, O. M. SMEDSTAD, J. CUMMINGS, G. R. HALLIWELL, R. BLECK, R. BARAILLE, A. J. WALLCRAFT, C. LOZANO, H. L. TOLMAN, A. SRINIVASAN, S. HANKIN, P. CORNILLON, R. WEISBERG, A. BARTH, R. HE, F. WERNER, AND J. WILKIN, 2009. U.S. GODAE: Global Ocean Prediction with the HYbrid Coordinate Ocean Model (HYCOM). *Oceanography*, **22**(2), 64–75.
- DEWAR, W. K., 1986: On the potential vorticity structure of weakly ventilated isopycnals: a theory of subtropical mode water maintenance. *J. Phys. Oceanogr.* **16**, 1204–1216.
- GOFF, J. A., 2020: Identifying characteristic and anomalous mantle from the complex relationship between abyssal hill roughness and spreading rates. *Geophys. Res. Lett.*, **47**, e2020GL088162.
- GOFF, J. A., AND T. H. JORDAN, 1988: Stochastic modeling of seafloor morphology: Inversion of sea beam data for second-order statistics. *J. Geophys. Res.*, **93**, 13,589–13,608.
- GOLDSMITH, E. J., AND J. G. ESLER, 2021: Wave propagation in rotating shallow water in the presence of small-scale topography. *J. Fluid Mech.*, **923**, A24.
- GULLIVER, L., AND T. RADKO, 2022: Topographic Stabilization of Ocean Rings. *Geophys. Res. Lett.*, **49**, e2021GL097686.
- HUGHES, C. W., AND B. A. DE CUEVAS, 2001: Why western boundary currents in realistic oceans are inviscid: A link between form stress and bottom pressure torques. *J. Phys. Oceanogr.*, **31**, 2871–2885.
- JACKSON, L., C. W. HUGHES, AND R. G. WILLIAMS, 2006: Topographic control of basin and channel flows: The role of bottom pressure torques and friction. *J. Phys. Oceanogr.*, **36**, 1786–1805.
- LACASCE, J., J. ESCARTIN, E. P. CHASSIGNET, AND X. XU, 2019: Jet instability over smooth, corrugated, and realistic bathymetry. *J. Phys. Oceanogr.*, **49**, 585–605.
- MARSHALL, D. P., WILLIAMS, R. G., AND LEE, M. M., 1999: The relation between eddy-induced transport and isopycnic gradients of potential vorticity. *J. Phys. Oceanogr.*, **29**, 1571–1578.
- MASHAYEK, A., 2023: Large-scale impacts of small-scale ocean topography. *J. Fluid Mech.*, **964**, F1.
- MEI, C. C., AND M. VERNESCU, 2010: *Homogenization methods for multiscale mechanics*. World Scientific Publishing, London.
- METZGER, E. J., O. M. SMEDSTAD, P. G. THOPPIL, H. E. HURLBURT, J. A. CUMMINGS, A. J. WALLCRAFT, L. ZAMUDIO, D. S. FRANKLIN, P. G. POSEY, M. W. PHELPS, P. J. HOGAN, F. L. BUB, AND C. J. DEHAAN, 2014: US Navy Operational Global Ocean and Arctic Ice Prediction Systems. *Oceanography*, **27**, 32–43.
- NIKURASHIN, M., R. FERRARI, N. GRISOUARD, AND K. POLZIN, 2014: The impact of finite-amplitude bottom topography on internal wave generation in the Southern Ocean. *J. Phys. Oceanogr.* **44**, 2938–2950.

- PALÓCZY, A., and J. H. LACASCE, 2022: Instability of a surface jet over rough topography. *J. Phys. Oceanogr.*, **52**, 2725–2740.
- PARSEVAL, M.-A., 1806: Mémoire sur les séries et sur l'intégration complète d'une équation aux différences partielles linéaires du second ordre, à coefficients constants. *Mém. prés. par divers savants. Acad. des Sciences, Paris*, **1**, 638–648.
- PEDLOSKY, J., 1987: *Geophysical Fluid Dynamics*, Springer.
- RADKO, T., 2020: Control of baroclinic instability by submesoscale topography. *J. Fluid Mech.*, **882**, A14.
- RADKO, T., 2022a: Spin-down of a barotropic vortex by irregular small-scale topography. *J. Fluid Mech.*, **944**, A5.
- RADKO, T., 2022b: Spin-down of a baroclinic vortex by irregular small-scale topography. *J. Fluid Mech.*, **953**, A7.
- RADKO, T., 2023a: A generalized theory of flow forcing by rough topography. *J. Fluid. Mech.*, **961**, A24.
- RADKO, T., 2023b: The sandpaper theory of flow-topography interaction for homogeneous shallow-water systems. *J. Fluid. Mech.*, **977**, A9.
- RADKO, T., 2024: The sandpaper theory of flow-topography interaction for multilayer shallow-water systems. *J. Fluid. Mech.*, **988**, A52.
- RHINES, P. B., and W. R. YOUNG, 1982: A theory of the wind-driven circulation. Part I: Mid-ocean gyres. *J. Mar. Res.*, **40** (Suppl), 559–596.
- STAMMER, D., 1997: Global characteristics of ocean variability estimated from regional TOPEX/Poseidon altimeter measurements, *J. Phys. Oceanogr.*, **27**, 1743–1769.
- STEWART, A. L., J. C. MCWILLIAMS, AND A. SOLODOCH, 2021: On the role of bottom pressure torques in wind-driven gyres. *J. Phys. Oceanogr.*, **51**, 1441–1464.
- VANNESTE, J., 2000: Enhanced dissipation for quasi-geostrophic motion over small-scale topography, *J. Fluid Mech.*, **407**, 105–122.
- VANNESTE, J., 2003. Nonlinear dynamics over rough topography: homogeneous and stratified quasi-geostrophic theory. *J. Fluid Mech.*, **474**, 299–318.